Supporting Information

Influence of Sn_{Bi} Antisite Defects on the Electronic Band Structure and Transport Properties of the Layered Chalcogenide Semiconductor $SnBi_2Te_4$

Ilayda Terzi,[1] Kacper Pryga,[2] Bartlomiej Wiendlocha,[2,*] Petr Levinský,[3] Soufiane El Oualid[1], Sylvie Migot[1], Jaafar Ghanbaja[1], Christine Gendarme[1], Thierry Schweitzer[1], Bernard Malaman,[1] Gérard Le Caër,[4] Bertrand Lenoir,[1] Christophe Candolfi[1,*]

[1] *Institut Jean Lamour, UMR 7198 CNRS – Université de Lorraine, 2 allée André Guinier-Campus ARTEM, BP 50840, 54011 Nancy Cedex, France*

[2] *AGH University of Krakow, Faculty of Physics and Applied Computer Science, Aleja Mickiewicza 30, 30-059 Krakow, Poland*

[3] *FZU – Institute of Physics of the Czech Academy of Sciences, Cukrovarnická 10/112, 162 00, Prague 6, Czech Republic*

[4] *Institut de Physique de Rennes, UMR UR1-CNRS 6251, Université de Rennes I, Campus de Beaulieu, 35042 Rennes Cedex, France*

[*]Contact authors: christophe.candolfi@univ-lorraine.fr ; wiendlocha@fis.agh.edu.pl

Content

4). Figure S4. Calculated power factor PF as a function of carrier concentration at T = 100, 300 and 700 K.

5). Figure S5. Fits of the Mössbauer spectrum by considering two models.

6). Figure S6. Dependence of the fitted quadrupole splitting QS(p) of the doublet when the singlet is assumed to originate from a proportion of Sn atoms p.

7). Additional discussion of the Mössbauer analysis.

8). Figure S7. Powder X-ray diffraction patterns of $Sn_{0.98(1)}Bi_{2.02(1)}Te_{3.99(1)}$ and $Sn_{0.99(1)}Bi_{2.00(1)}Te_{4.01(1)}$ collected before and after annealing on bulk pieces.

9). Figures S8 to S10. Rietveld refinements of the PXRD patterns of $Sn_{0.98(1)}Bi_{2.02(1)}Te_{3.99(1)}$ and $Sn_{0.99(1)}Bi_{2.00(1)}Te_{4.01(1)}$ annealed for 10 days and of the $SnBi_2Te_4$ sample annealed for 75 days.

10). Figure S11. X-ray diffraction patterns collected on bulk pieces cut parallel and perpendicular to the pressing direction.

11). Figure S12. SEM images in backscattered electron (BSE) mode and the corresponding elemental mapping from EDXS of $Sn_{0.98(1)}Bi_{2.02(1)}Te_{3.99(1)}$ and $Sn_{0.99(1)}Bi_{2.00(1)}Te_{4.01(1)}$.

12). Figure S13. STEM images collected on the $Sn_{0.99(1)}Bi_{2.00(1)}Te_{4.01(1)}$ and $Sn_{0.98(1)}Bi_{2.02(1)}Te_{3.99(1)}$ annealed for 10 days.

13). Figure S14. HAADF-STEM image taken on the $Sn_{0.98(1)}Bi_{2.02(1)}Te_{3.99(1)}$ sample annealed for 10 days.

14). Figure S15. HAADF-STEM images collected on the $Sn_{0.99(1)}Bi_{2.00(1)}Te_{4.01(1)}$ and $Sn_{0.98(1)}Bi_{2.02(1)}Te_{3.99(1)}$ samples annealed for 10 days, indicating the presence of double layers.

15). Figure S16. Bright-field images (BF) and corresponding elemental X-ray maps for the $Sn_{0.99(1)}Bi_{2.00(1)}Te_{4.01(1)}$ and $Sn_{0.98(1)}Bi_{2.02(1)}Te_{3.99(1)}$ samples annealed for 10 days.

16). Figure S17. Comparison of the transport properties of $SnBi_2Te_4$ samples annealed for 10 and 75 days.

17). Figure S18. Energy dependent mobility ratio for electrons and holes in $SnBi_2Te_4$.

18). Figure S19. Comparison of the energy dependent mobility ratio for electrons and holes in Sn_{Bi}-containing $SnBi_{1.958}Sn_{0.042}Te_4$ to the pure $SnBi_2Te_4$.

19). Figure S20. Comparison of the calculated and measured $\alpha(T)$ curves for a reduced band gap of 23 meV.

20). Figure S21. Electronic density of states (DOS) and calculated thermopower with the presence of Bi_{Sn} antisite defects.

21). Figure S22. Effect of Sn vacancy on the electronic density of states (DOS) of $SnBi_2Te_4$.

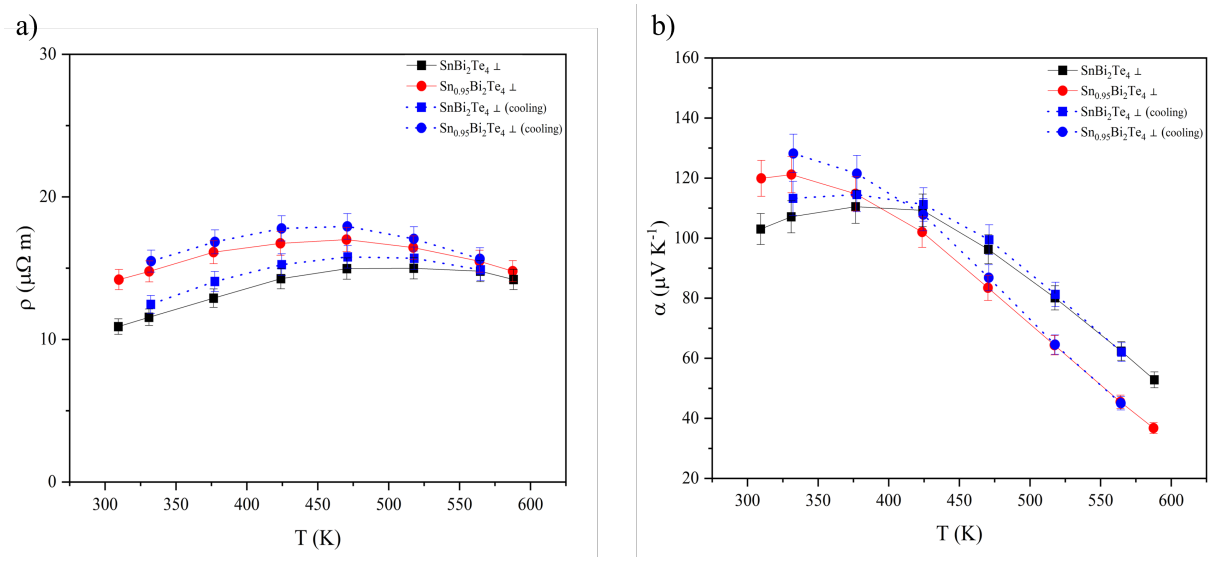

Figure S1. Temperature dependence of the a) electrical resistivity and b) thermopower measured upon heating and cooling for $Sn_{0.99(1)}Bi_{2.00(1)}Te_{4.01(1)}$ and $Sn_{0.98(1)}Bi_{2.02(1)}Te_{3.99(1)}$ annealed for 10 days. The data were measured on samples cut perpendicularly to the pressing direction.

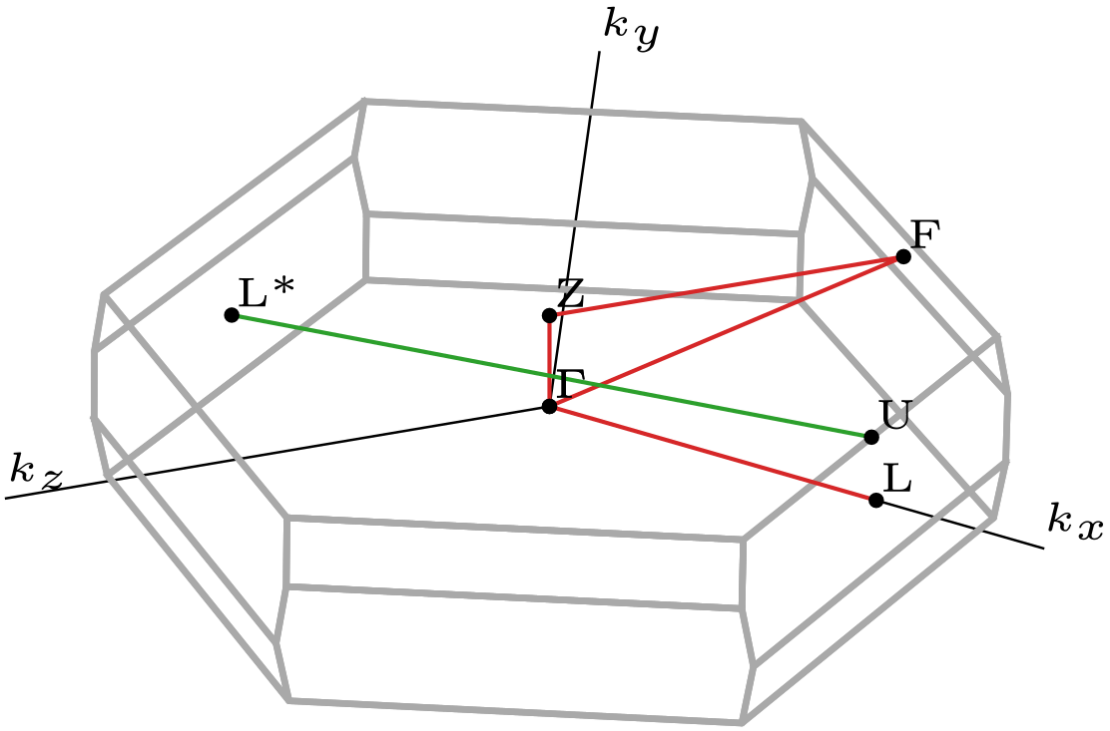

Figure S2. Brillouin zone with marked paths used for electronic band structure calculations.

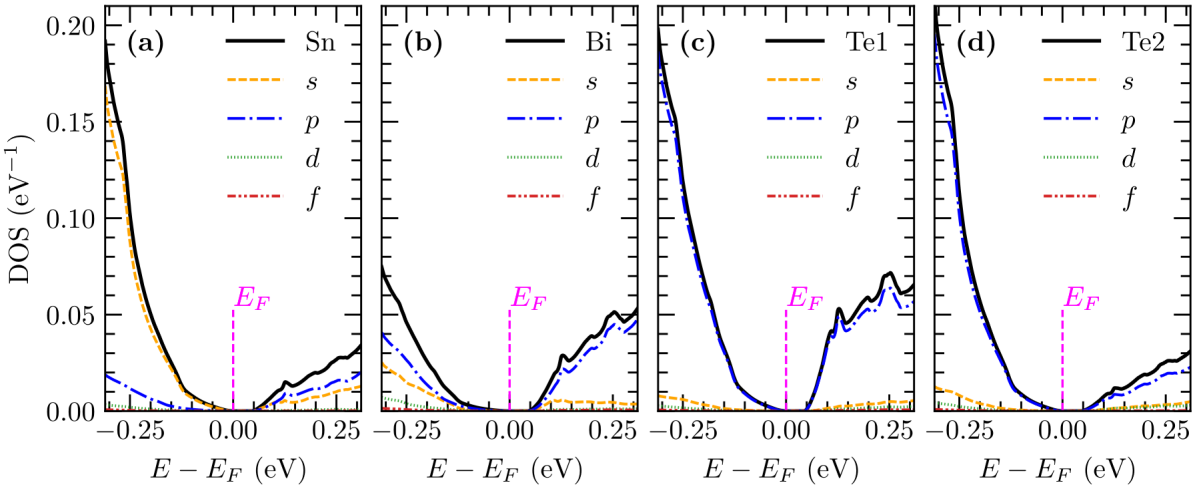

Figure S3. Calculated partial density of states of $SnBi_2Te_4$ with orbital decomposition. Partial DOS is given per atom.

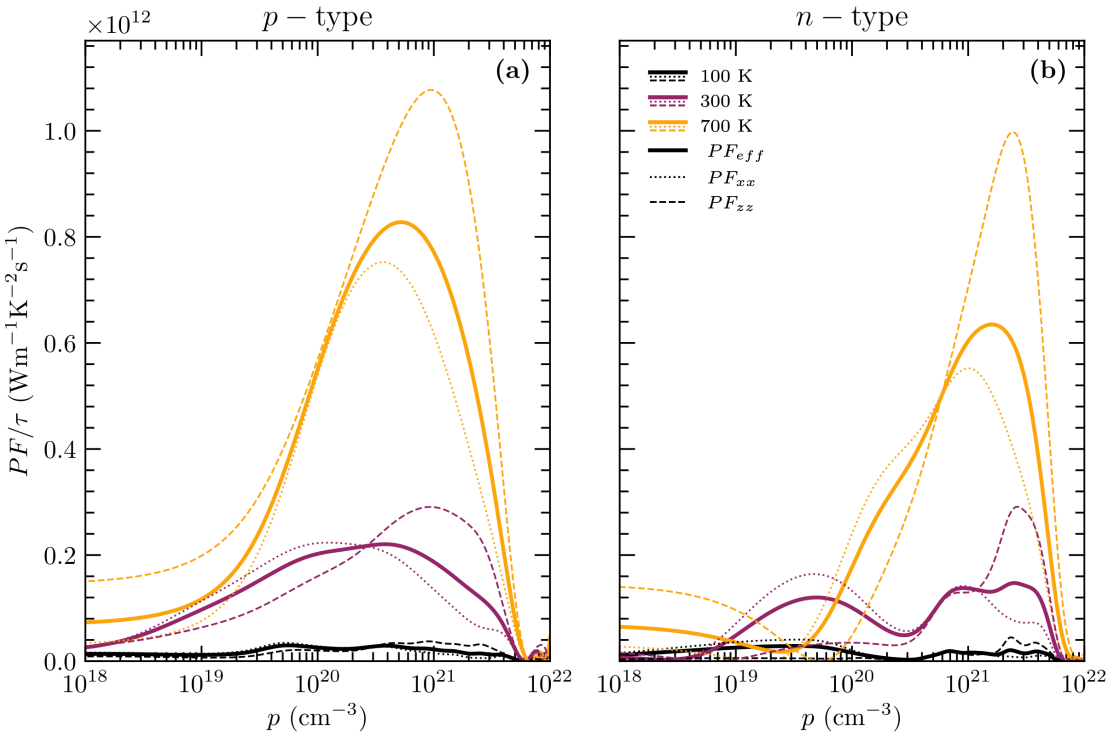

Figure S4. Calculated power factor *PF* divided by the relaxation time τ as a function of carrier concentration at T = 100, 300 and 700 K.

Effective values of power factor $PF = \alpha^2/\rho$, shown in Figure S4 as a function of the carrier concentration and corresponding to a polycrystalline material, have been approximated using the parallel grain model

$$PF_{eff} = \frac{1}{3}\left(\alpha_{xx}^2\sigma_{xx} + \alpha_{yy}^2\sigma_{yy} + \alpha_{zz}^2\sigma_{zz}\right) \quad \text{(S1)}$$

From the effective values of *PF*, the optimal carrier concentration range to maximize it in *p*-type $SnBi_2Te_4$ is in the range 4 – 6×10^{20} cm^{-3}. Considering electron-doped $SnBi_2Te_4$, the optimum electron concentration is much higher, around 9×10^{20} – 2.5×10^{21} cm^{-3}, where a plateau in *PF* is visible, especially at 300 K. Near this optimal *n*, the PF_{zz} component has the highest values, in agreement with the calculations of α.

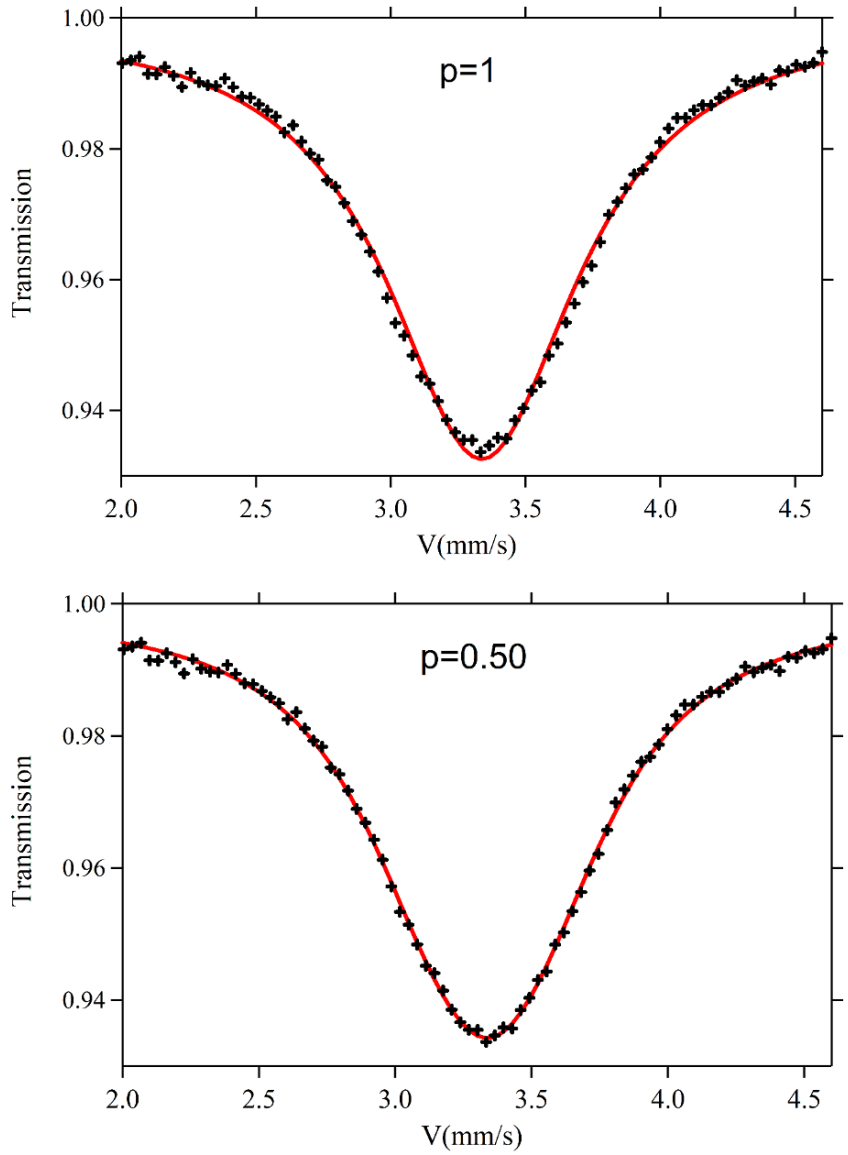

Figure S5. The main peak of the experimental spectrum of $SnBi_2Te_4$ measured at 15 K (see Figure 10 in the main text for the full spectrum) in a velocity range suited for a comparison of fits with a single line (p = 1) or with a single line and a doublet of lines of equal weights (p = 0.5).

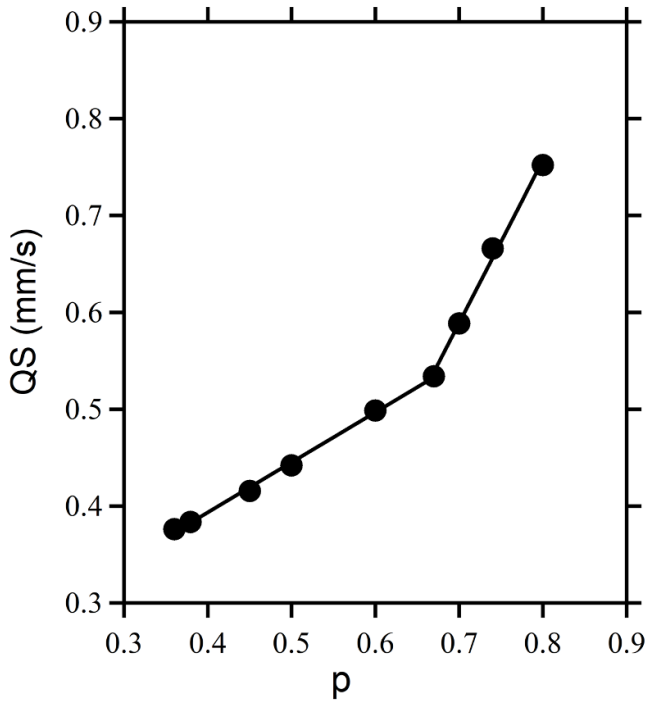

Figure S6. Quadrupolar splitting (QS) as a function of the proportion of Sn atoms *p*.

Additional discussion on the Mössbauer analysis: Does the main ^{119}Sn Mössbauer peak consists of a single line or of a single line and a doublet of lines?

We recall first that each Sn atom occupies a symmetrical octahedron formed by six Te1 atoms with Sn-Te interatomic distances of 3.10 Å. Bi atoms occupy distorted octahedral formed by three Te1 and three Te2 atoms. The corresponding interatomic distances are 3.40 Å and 3.08 Å, respectively. Evidence for antisite Sn atoms occupying Bi positions in single-crystalline $SnBi_2Te_4$ nanoplates, grown by chemical vapor deposition, were reported by Zou *et al*. (S1). According to this study, defect energy calculations reveal that such antisites have a low formation energy.

The Figure 10 in the main text shows an experimental ^{119}Sn Mössbauer spectrum of $Sn_{0.99(1)}Bi_{2.00(1)}Te_{4.01(1)}$ measured at 15 K in a velocity range that shows first a small broad component close to 0 mm s^{-1}, attributed to SnO_2, which has been discussed in detail in the text

and will not be further considered here. We focus below on the main component ascribed to $Sn_{0.99(1)}Bi_{2.00(1)}Te_{4.01(1)}$. The latter symmetrical component has its maximum absorption at 3.34±0.04 mm s^{-1}, a value associated with Sn^{+2} oxidation states.

For a perfectly ordered distribution of Sn atoms, the ^{119}Sn Mössbauer spectrum consists of a single line, because of the symmetrical environment of Sn atoms. A single line, associated with a fraction p of Sn atoms ($p < 1$), and a doublet of lines are instead expected if a fraction 1-p of Sn atoms occupies Bi positions. The asymmetrical environments of Bi sites occupied then by Sn atoms would suggest that the quadrupole splitting of the latter doublet might be significant provided that Sn atoms do not distort their local Te environments. Only theoretical calculations might indicate what occurs. However, the shape of the main peak of the spectrum, shown in Figures S2 and S3, imposes constraints, discussed below, on the characteristics of the antisite contribution to the main peak. We investigated the two cases described below to know if an optimal spectral fitting exists for some value of $p = p^*$, when p varies in a broad range. Only p^* has a physical meaning if an optimum is veritably found.

I. Fit of the main component with a single peak ($p = 1$)

A least-squares fit of the experimental spectrum (Figure S2) yields a single Lorentz line at 3.34±0.01 mm s^{-1} for the main component. Its full-width at half-maximum (FWHM) is Γ = 0.86±0.01 mm s^{-1} (Figure S2, $p = 1$). This FWHM is reasonable when compared to those published for a variety of tin compounds. We notice that the minimum possible FWHM value is $\Gamma(0)$ = 0.703±0.012 mm s^{-1} which is obtained from FWHM's, measured for various amounts (the so-called Mössbauer thicknesses "*t*" which depend too on Lamb-Mössbauer factors "*f*") of Sn in barium stannide and extrapolated to zero amount of Sn (Ref. S3). Most often, line broadenings with respect to $\Gamma(0)$ cannot be estimated. Indeed, sample thicknesses "*t*" are seldomly given in published papers and the "*f*"'s have generally unknown values.

II. Fits of the main component with a single peak and a doublet of peaks ($p < 1$)

FWHM's are assumed to be identical for the three lines when fitting spectra. Their values are found to be independent of p, $\Gamma(p) = 0.73 \pm 0.02$ mm s^{-1} for $0.36 \leq p \leq 0.80$. Identical isomer shifts, within experimental errors, consistent with the symmetrical shape of the main line, are obtained for the singlet and for the doublet for any value of p. The quadrupole splitting QS(p), where p is fixed in the fitting process, depends on the assumed value of p as shown in Figure S3. Figure S3 shows that the slope of QS(p) as a function of p increases strongly (from 0.51 to 1.68) when p becomes larger than ~0.65. QS(p), as a whole, has no physical meaning as only QS(p*), with p* defined above, would have such a meaning. Nevertheless, relevant information may be obtained from the variation of QS(p) in the investigated range of p. For instance, let us imagine that QS(p) would be constant or that it would vary only slightly with p.

Figure S2 shows the main peak of the experimental spectrum of $Sn_{0.99(1)}Bi_{2.00(1)}Te_{4.01(1)}$ at 15 K (Figure 10) in a velocity range suited for a comparison of fits with a single line ($p = 1$) or with a singlet and a doublet of respective weights p and 1-p (p = 0.8, 0.7 and 0.5) The quality of fits is similar for $p = 1$ and $p = 0.8$. The quality of the fit performed for $p = 0.7$ is intermediate between those of the latter fits and the best fits, essentially undistinguishable, found in the range of p, $0.36 \leq p \leq 0.67$ which was considered (examples are given in Figure S2). These best fits are however found with a larger number of degrees of freedom, i.e. of free fitting parameters.

Using the parameters of Table IV of Ref. S2, we simulated a ^{119}Sn Mössbauer spectrum, using a pseudo-random number generator to produce count rate fluctuations similar to those shown in Figure 7a of Ref. S2, smaller than those of Figure S2. This simulated spectrum was fitted in the same way as our experimental spectrum. The evolution of fits with p was similar to the one described above. These results confirm that the observed evolution with p is intrinsic to the shape of the main peak.

III. Conclusions

Either the fraction of antisite Sn atoms is large >~0.3, a region of *p* with the best fits and quadrupole splitting ~0.45±0.07 mm s^{-1}, or the fraction of antisite Sn atoms is moderate to small (<~0.3) and quadrupole splitting values are somewhat larger, ~ 0.67±0.08 mm s^{-1}. In any case, these values are not so large for *a priori* strongly distorted octahedral sites.

Strictly speaking, it would be difficult to distinguish between a perfectly ordered distribution of Sn atoms and a distribution with a fraction of Sn antisites smaller than ~ 0.2 to 0.3. However, combining these analyses with energy-defect calculations performed by Zou *et al*. (Ref. S1) and our transport calculations (see the main text), the presence of Sn_{Bi} antisite defects in $SnBi_2Te_4$ is very likely.

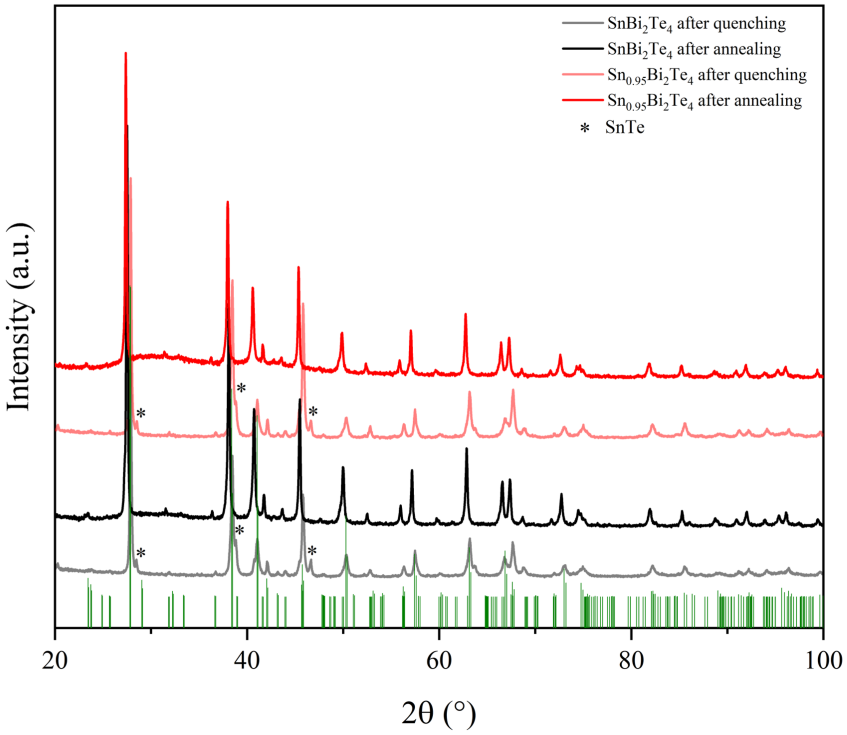

Figure S7. Powder X-ray diffraction patterns of the $Sn_{0.98(1)}Bi_{2.02(1)}Te_{3.99(1)}$ and $Sn_{0.99(1)}Bi_{2.00(1)}Te_{4.01(1)}$ compounds collected before and after annealing for 10 days.

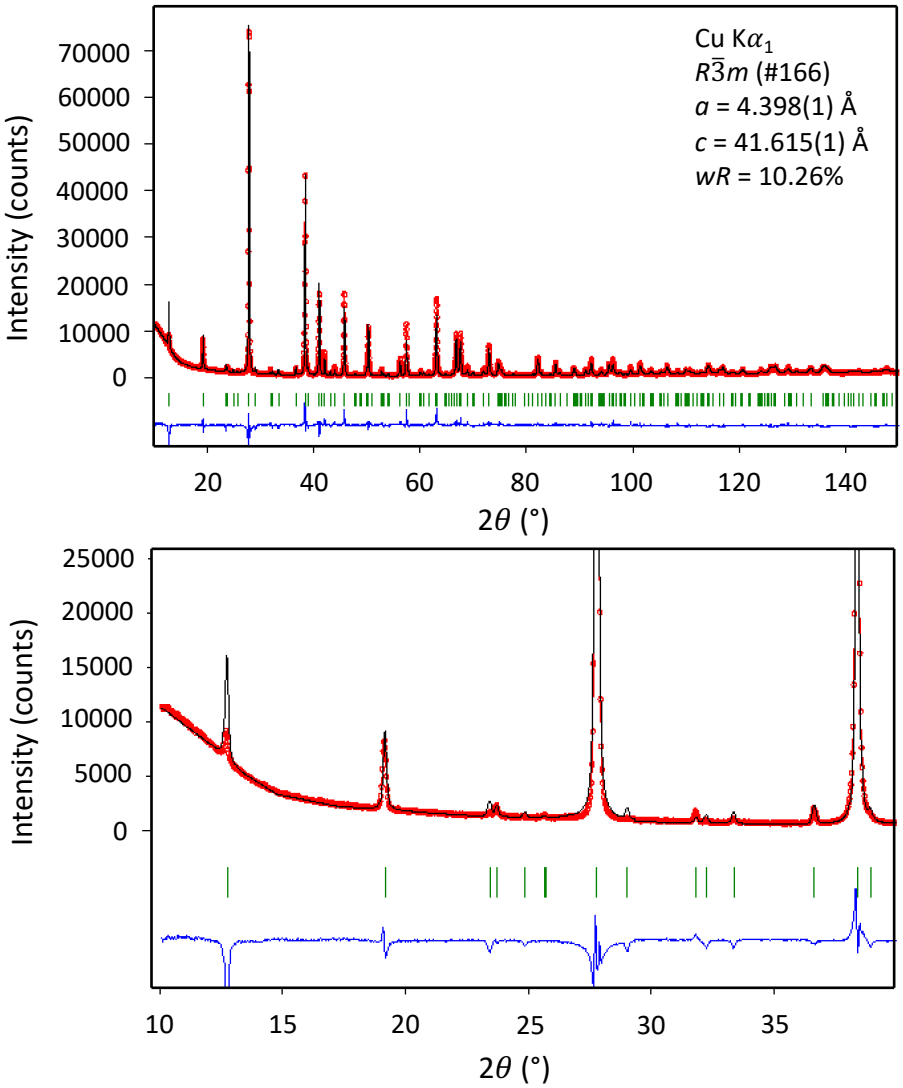

Figure S8. (upper panel) Rietveld refinement of the PXRD pattern of the $SnBi_2Te_4$ compound considering an ordered model. (lower panel) Magnification of the refinement at low angles.

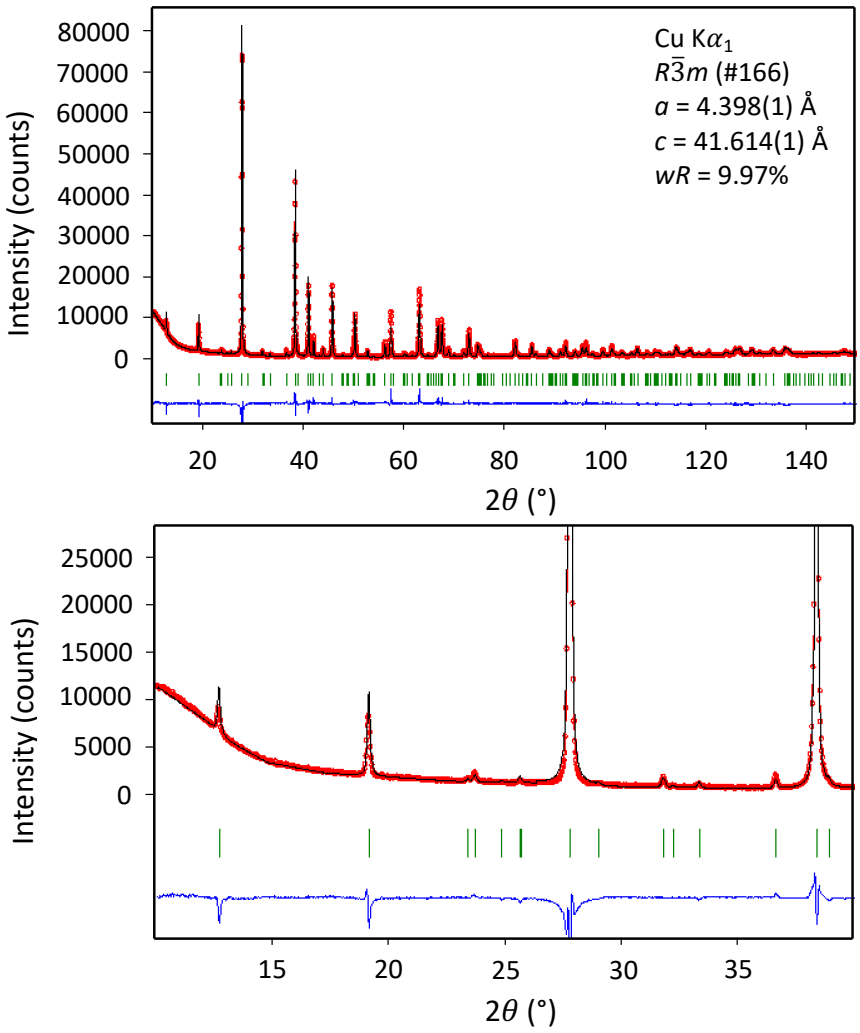

Figure S9. (upper panel) Rietveld refinement of the PXRD pattern of the $SnBi_2Te_4$ compound with Sn/Bi mixing allowed to be refined. (lower panel) Magnification of the refinement at low angles.

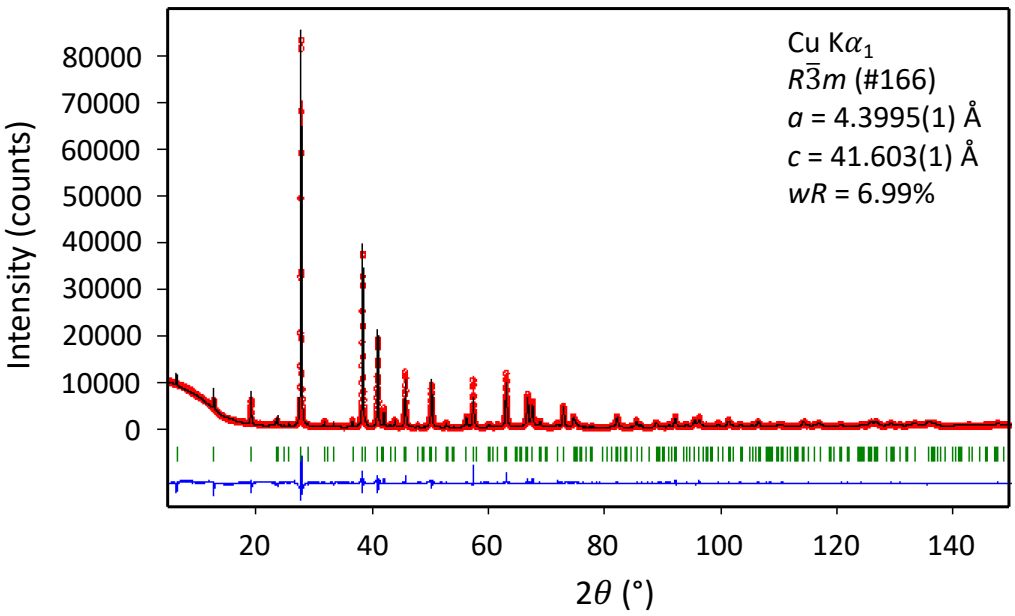

Figure S10. Rietveld refinement of the PXRD pattern of the $SnBi_2Te_4$ sample annealed for 75 days using an ordered model.

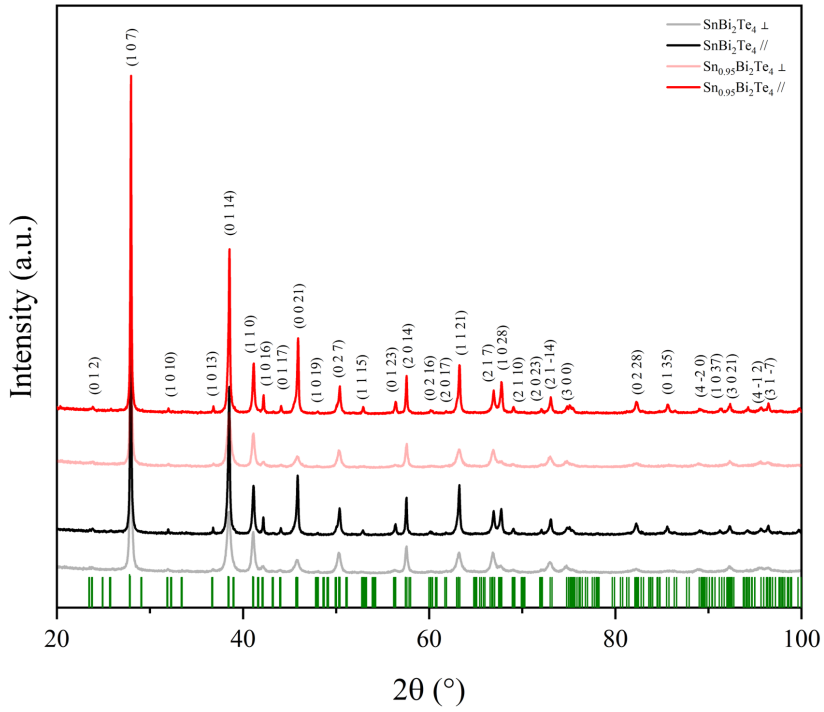

Figure S11. Powder X-ray diffraction patterns collected on bulk pieces of the $Sn_{0.98(1)}Bi_{2.02(1)}Te_{3.99(1)}$ and $Sn_{0.99(1)}Bi_{2.00(1)}Te_{4.01(1)}$ compounds annealed for 10 days cut parallel and perpendicular to the pressing direction.

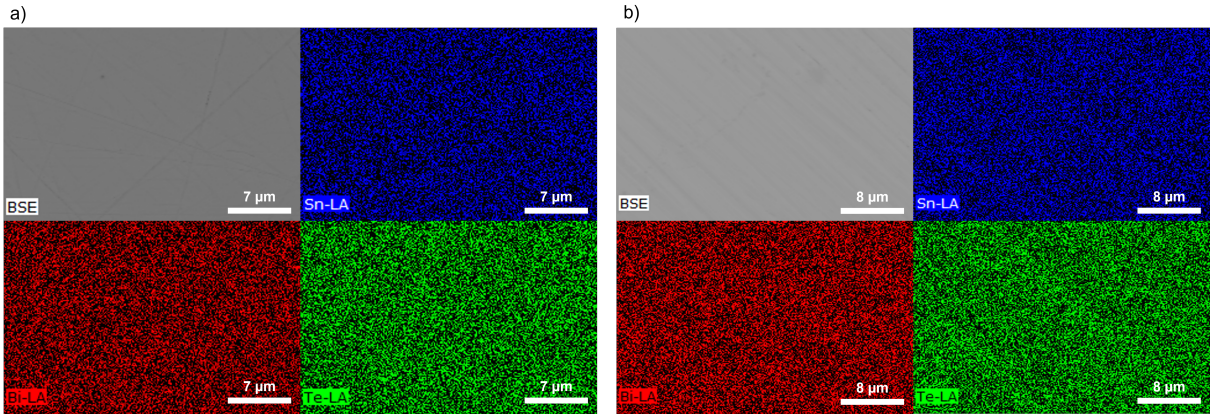

Figure S12. SEM images in backscattered electron (BSE) mode and the corresponding elemental mapping from EDXS of a) $Sn_{0.98(1)}Bi_{2.02(1)}Te_{3.99(1)}$ and b) $Sn_{0.99(1)}Bi_{2.00(1)}Te_{4.01(1)}$. Both samples were annealed for 10 days.

Additional STEM analyses and discussion

While the results of PXRD, EPMA and SEM are all consistent with the expected crystal structure and stoichiometry of $SnBi_2Te_4$, TEM analyses reveal a more complex situation for samples annealed for 10 days. Typical STEM images (Figures S13a to S13d), taken along the [100] direction, reveal the presence of a large number of stacking faults. As a result, the infinite sequence of septuple layers, is not observed over extended areas. This is further corroborated by the corresponding selected area electron diffraction (SAED) patterns in which extended streaks along the c^* direction can be observed, reflecting the presence of short-range defects along the c axis. Additionally, two types of electron diffraction patterns are observed for both samples depending on the studied area (Fig. S13e and S13f). The strongest reflections in these patterns are consistent with the rhombohedral symmetry of the crystal lattice. A second set of intermediate, weaker-intensity reflections running along the c^* direction is either consistent with that predicted for $SnBi_2Te_4$, with the presence of six reflections evenly spaced corresponding to the (000*l*) reflections from (0003) to (00021), or differs with the presence of

only two reflections in addition to satellite reflections on either side of the main ones (Fig. S13g and S13h). The distance between the main and satellite reflections of 0.0483 $Å^{-1}$ is lower than the expected distance of 0.0714 $Å^{-1}$ for the evenly-spaced case, suggesting the presence of an incommensurate modulation along the *c* axis, possibly being fully disordered or forming a composite structure that can be represented as several intergrown sublattices. This stacking complexity is further evidenced by the presence of double and nine-atom-thick layers in both samples (see Figure S14 below). Double layers, in addition to quintuple and septuple layers, have also been observed in the pseudo-binary system $(SnSe)_x(Bi_2Se_3)$, giving rise to commensurate structures with very long periodicities and lattice parameters *c* of up to 282 Å (Ref. 66 in the main text). Similar diffraction patterns have also been observed in other homologous series such as $(Bi_2)_n(Bi_2X_3)_m$ (X = Se or Te) or $(GeTe)(Bi_2Te_3)_n$, which have been interpreted in terms of either commensurate or incommensurate modulated structures depending on the chemical composition (Refs. 67 and 68 in the main text). Complex stacking sequences are typical of infinitely adaptive structures where slight variations in the chemical composition can lead to distinct crystal structures. Quintuple layers are also visible in $Sn_{0.98(1)}Bi_{2.02(1)}Te_{3.99(1)}$, indicative of an intergrowth between $SnBi_2Te_4$ and the line compound $SnBi_4Te_7$ for which seven- and quintuple-layers are stacked with the sequence 7–5–7 (see Fig. 1 in the main text). The presence of $SnBi_4Te_7$ is consistent with the EPMA results and the pseudo-binary $Sn_{1-\delta}Te$–Bi_2Te_3 phase diagram (Ref. 32 in the main text), suggesting that high nominal Sn deficiency cannot be accommodated by the crystal structure and results in the intergrowth of $SnBi_4Te_7$ as a secondary phase.

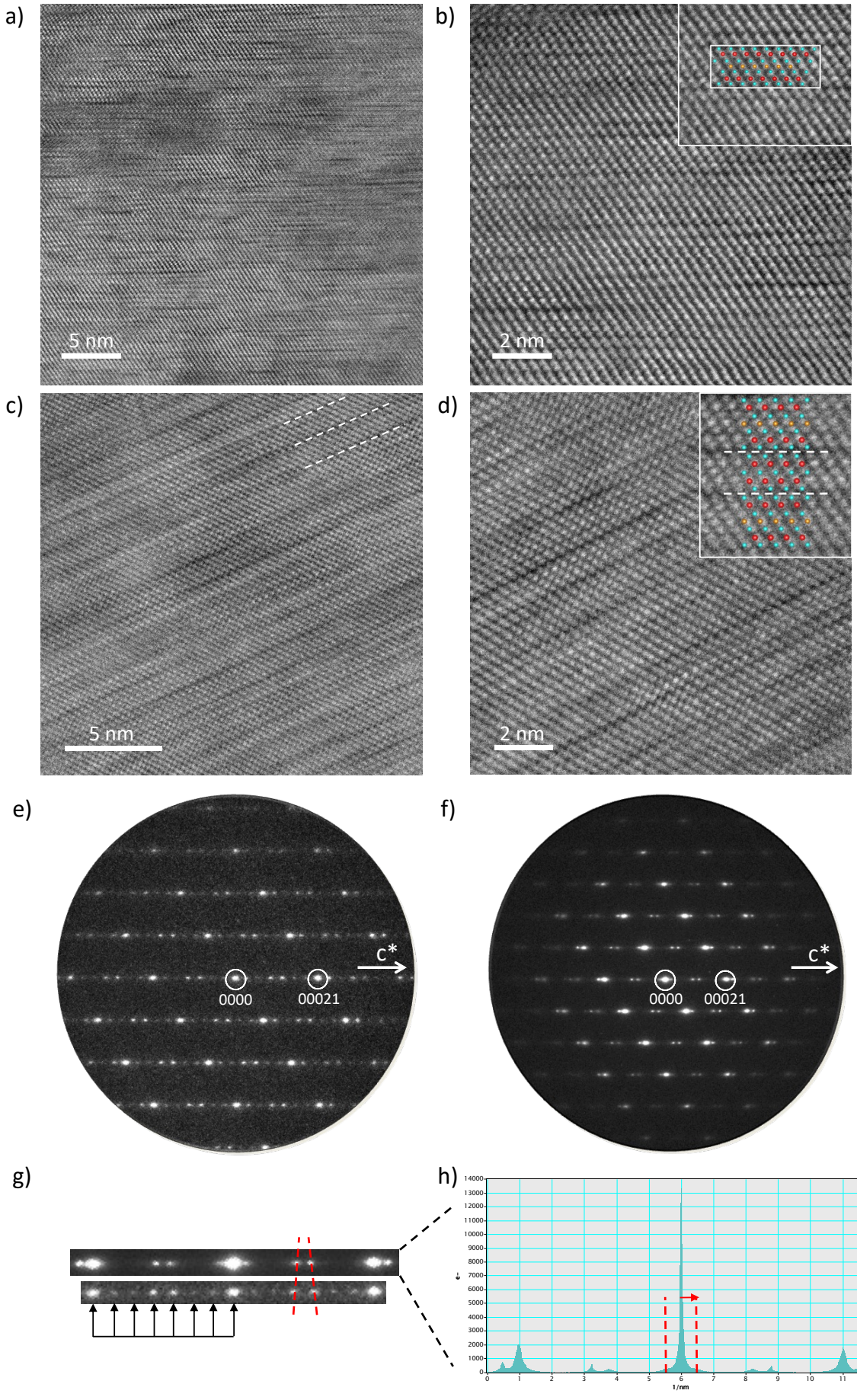
a)
5 nm
b)
2 nm
c)
5 nm
d)
2 nm
e)
c*
0000
00021
f)
c*
0000
00021
g)
h)
1/nm

Figure S13. STEM images collected on the $Sn_{0.99(1)}Bi_{2.00(1)}Te_{4.01(1)}$ (a and b) and $Sn_{0.98(1)}Bi_{2.02(1)}Te_{3.99(1)}$ (c and d). The inset of b) shows a fragment (one septuple layer) of the crystal structure of $SnBi_2Te_4$ overlaid. The white dashed lines in c) highlight a region where the expected regular 7–7 stacking sequence is observed. The inset of d) shows a fragment (one quintuple layer sandwiched by two septuple layers) of the crystal structure of $SnBi_4Te_7$ indicative of the intergrowth of $SnBi_2Te_4$ and $SnBi_4Te_7$. SAED patterns corresponding e) to the regular 7–7 stacking sequence and f) to the disordered or incommensurate modulated structure. In both patterns, the two main (000*l*) reflections are indicated. g) Difference between the two (000*l*) rows of reflections of the disordered (upper row) and regular pattern (bottom row) highlighted by the two dashed red lines showing the shift of these reflections. The evenly-spaced six reflections of the 7–7 stacking sequence are indicated by the black arrows (bottom row). h) Intensity profile corresponding to the disordered structure (upper row) showing the presence of satellite reflections, with the possible corresponding modulation vector indicated by the horizontal red arrow.

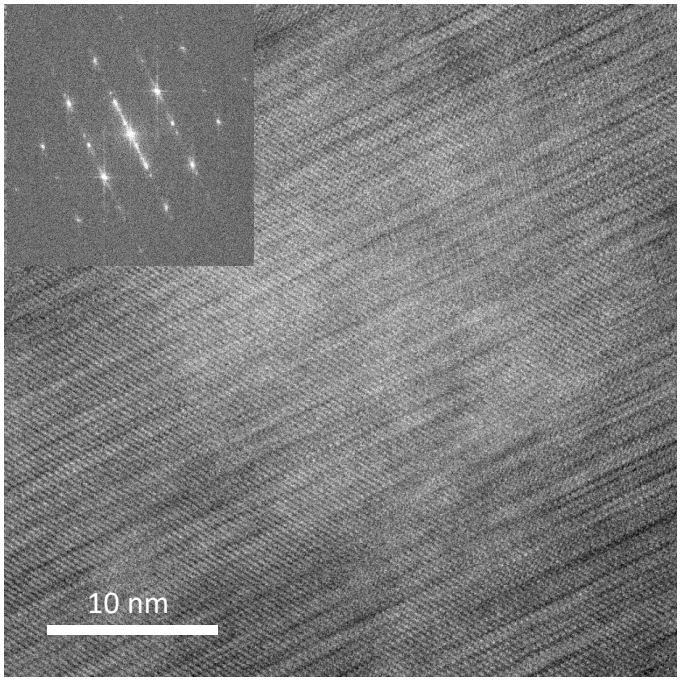

Figure S14. HAADF-STEM image taken on the $Sn_{0.98(1)}Bi_{2.02(1)}Te_{3.99(1)}$ sample at low magnification, evidencing the presence of stacking faults that lead to streaks extending along the *c* axis, as shown by the corresponding SAED pattern in the inset.

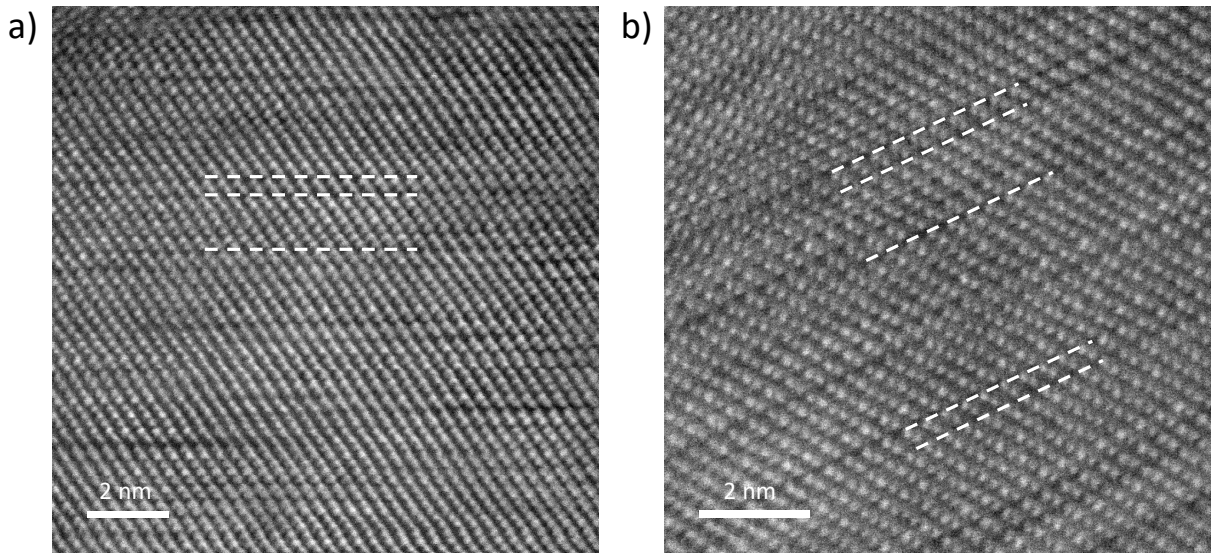

Figure S15. HAADF-STEM images collected on the a) $Sn_{0.99(1)}Bi_{2.00(1)}Te_{4.01(1)}$ and b) $Sn_{0.98(1)}Bi_{2.02(1)}Te_{3.99(1)}$ samples, indicating the presence of double layers intercalated between septuple layers (delineated by the white dashed lines).

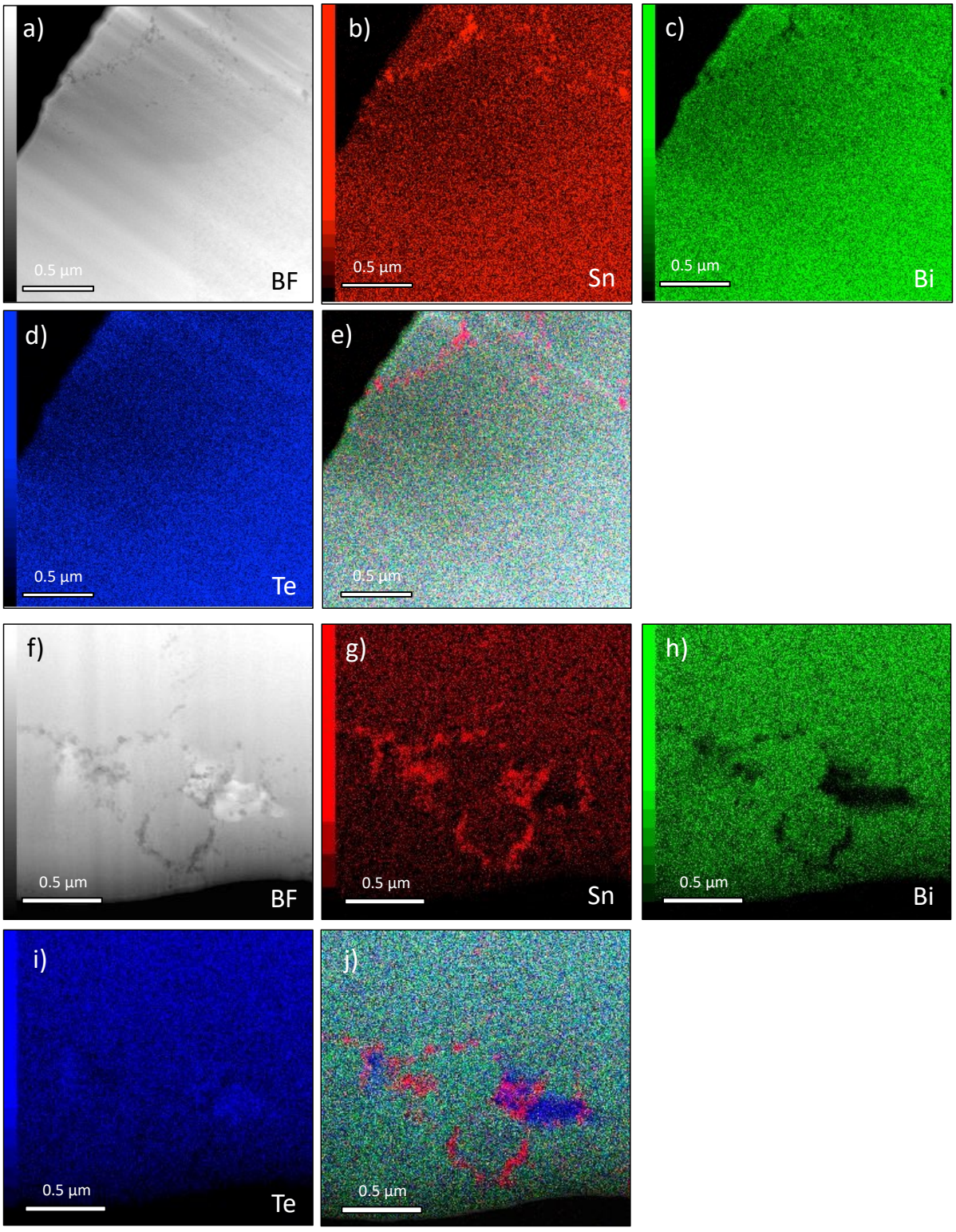

Figure S16. Bright-field images (BF) and corresponding elemental X-ray maps for (a to e) $Sn_{0.99(1)}Bi_{2.00(1)}Te_{4.01(1)}$ and (f to j) $Sn_{0.98(1)}Bi_{2.02(1)}Te_{3.99(1)}$ annealed for 10 days obtained by scanning transmission electron microscopy (STEM). Images e) and j) shows an overlay of the X-ray maps of the three elements.

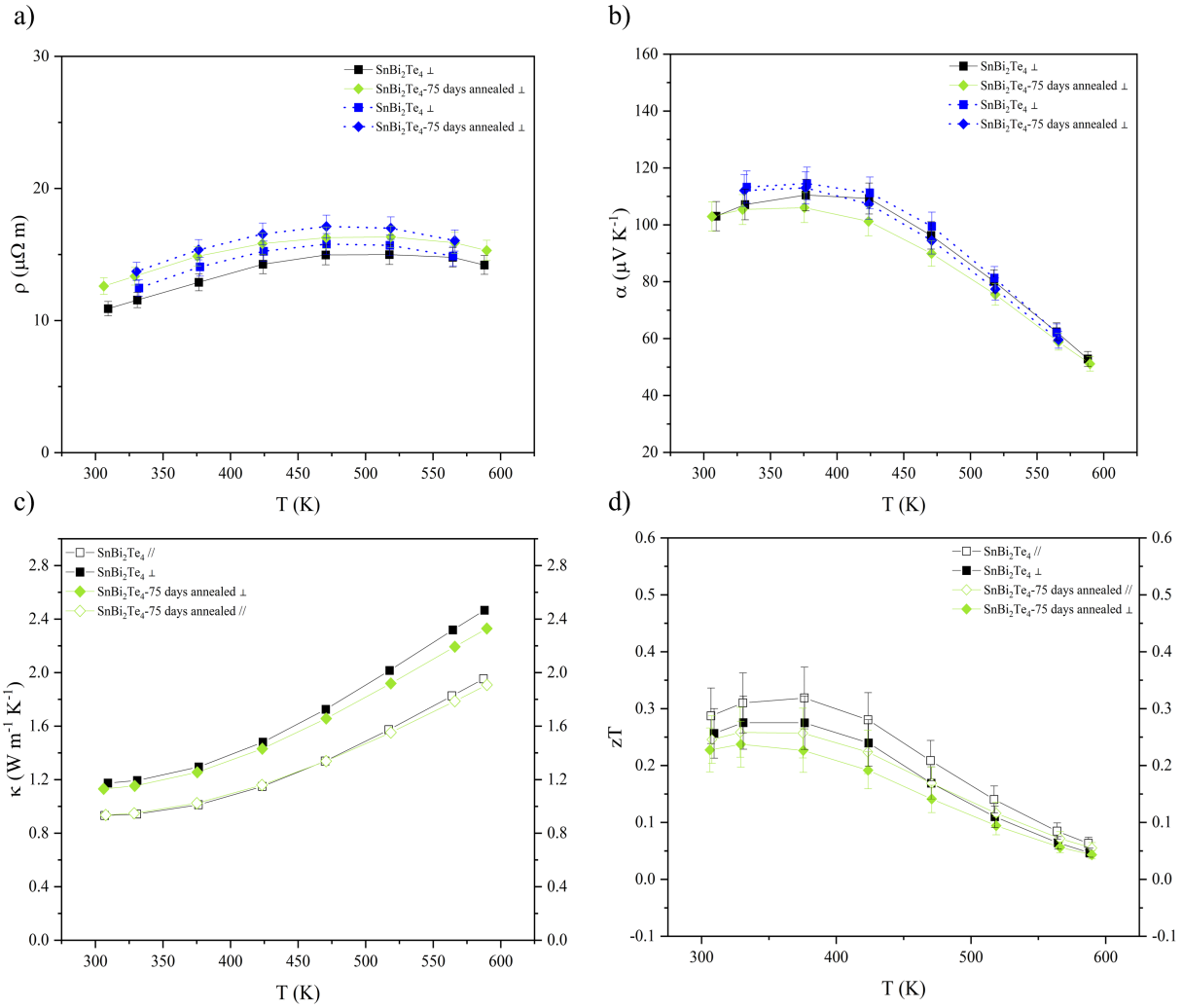

Figure S17. Comparison of the temperature dependence of the a) electrical resistivity ρ, b) thermopower α, c) total thermal conductivity κ and dimensionless thermoelectric figure of merit ZT for $SnBi_2Te_4$ annealed for 10 and 75 days. For clarity, only the measurements performed along the perpendicular direction are shown for ρ and α, while both data sets are shown for κ and ZT.

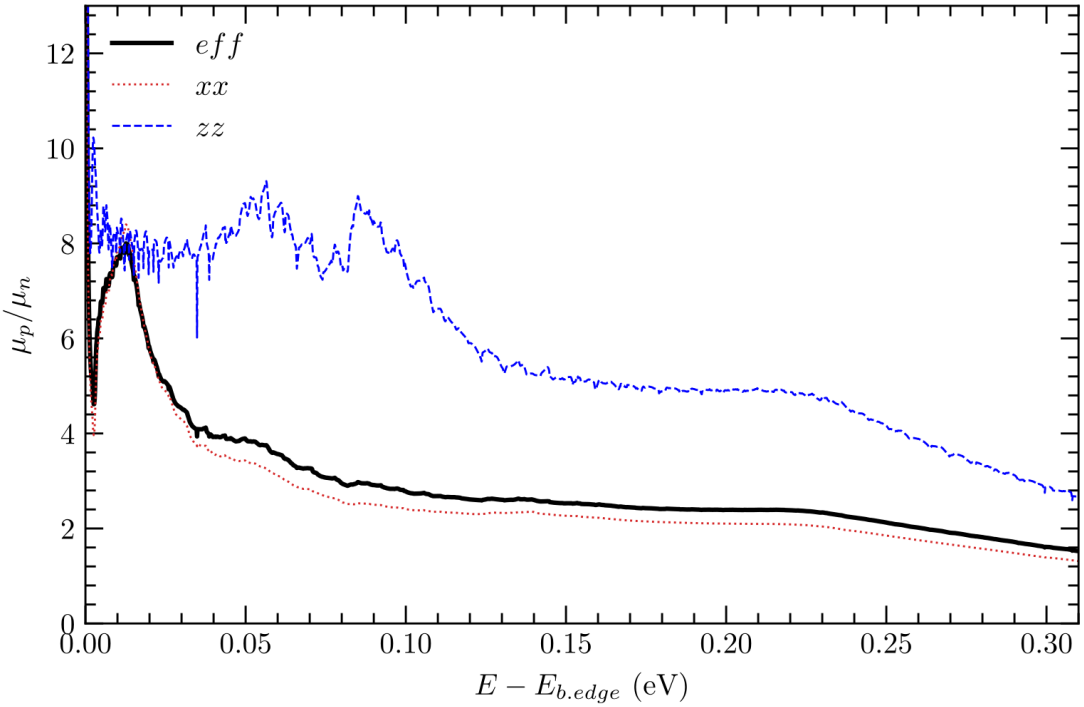

Figure S18. Calculated energy dependent mobility ratio for holes and electrons (average and along in plane *'xx'* and trigonal *'zz'* directions) in $SnBi_2Te_4$, showing the asymmetry of the transport properties between the valence and conduction bands, which promote the *p*-type thermoelectric transport.

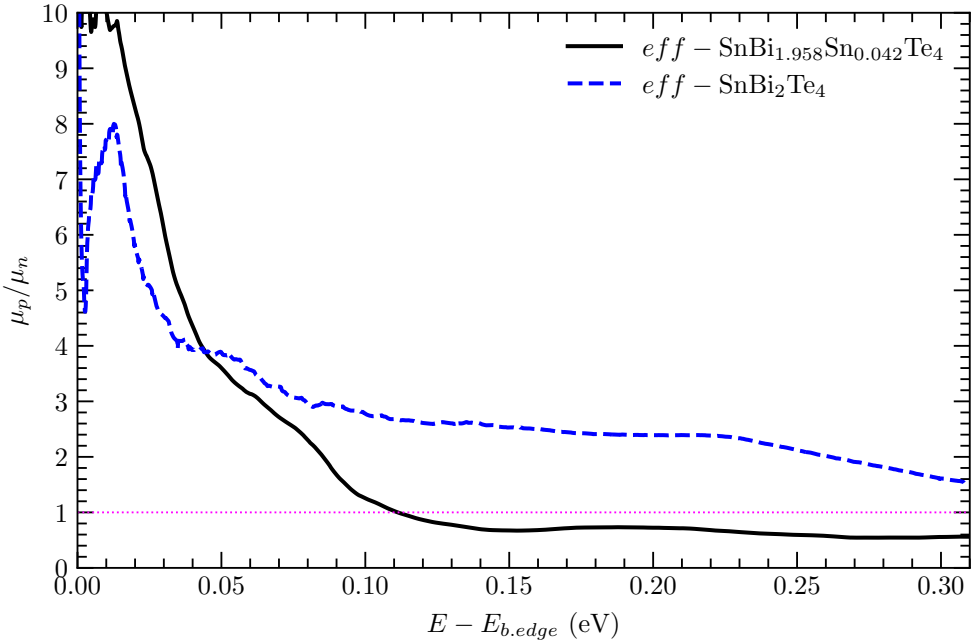

Figure S19. Calculated energy dependent mobility ratio for holes and electrons (average) in $SnBi_{1.958}Sn_{0.042}Te_4$ (that is, with the presence of Sn_{Bi} antisites), compared to $SnBi_2Te_4$. The presence of Sn_{Bi} antisite defects changes the asymmetry of the transport properties between the valence and conduction bands, as the mobility ratio quickly drops below 1.0, which promotes the *n*-type thermoelectric transport and leads to a strong bipolar effect in *p*-type samples.

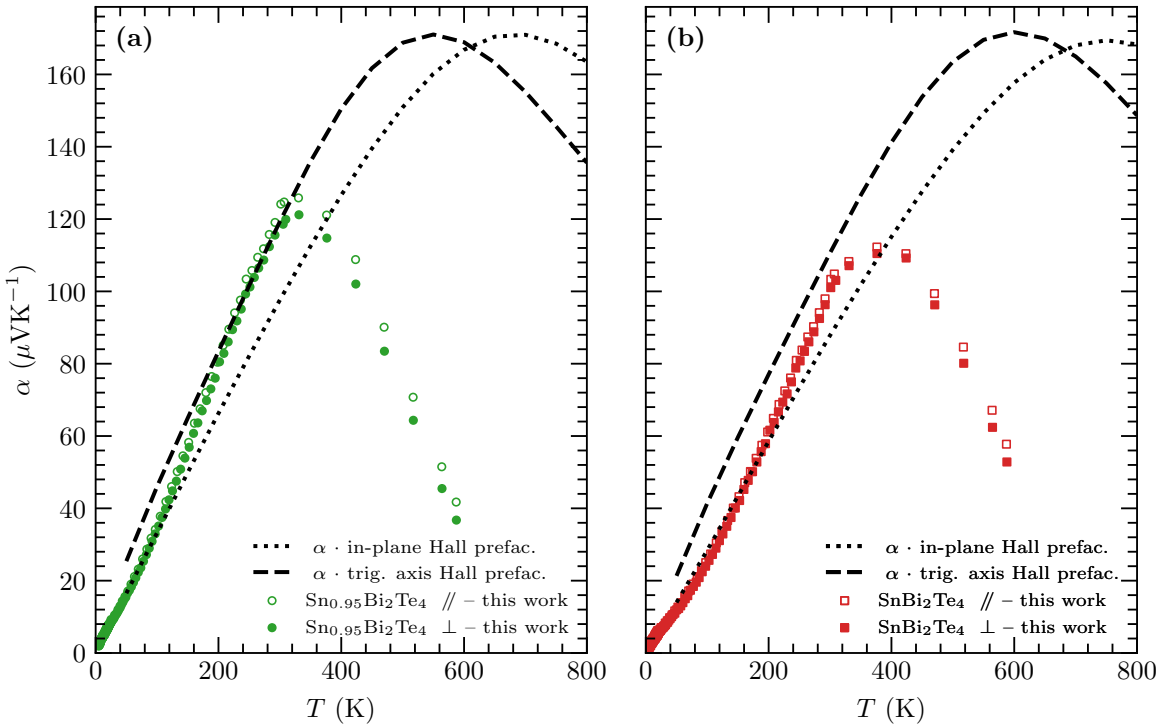

Figure S20. Thermopower as a function of temperature: comparison of the experimental results with the calculated curves for the reduced band gap of 23 meV. The disagreement shows that a sole reduction of the band gap does not explain the experimental results, supporting the hypothesis of the dominating Sn_{Bi} antisite defects, which reduce the band gap and affect the mobility ratio.

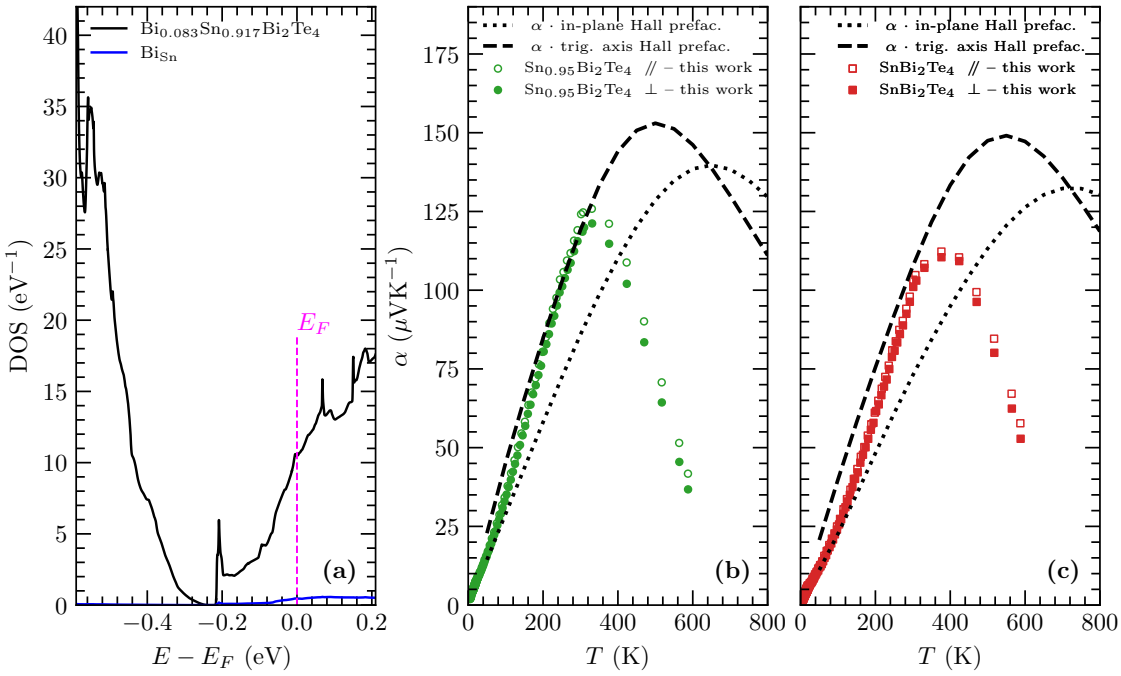

Figure S21. (Left panel) Electronic density of states (DOS) of supercell $Bi_{0.083}Sn_{0.917}Bi_2Te_4$. (Right panels) Calculated thermopower for carrier concentrations corrected for the Hall factor as a function of temperature. The calculated trend in $\alpha(T)$ does not explain the experimental results, showing that Bi_{Sn} antisite defects are not the main type of defects, supporting the hypothesis of the dominating Sn_{Bi} antisites.

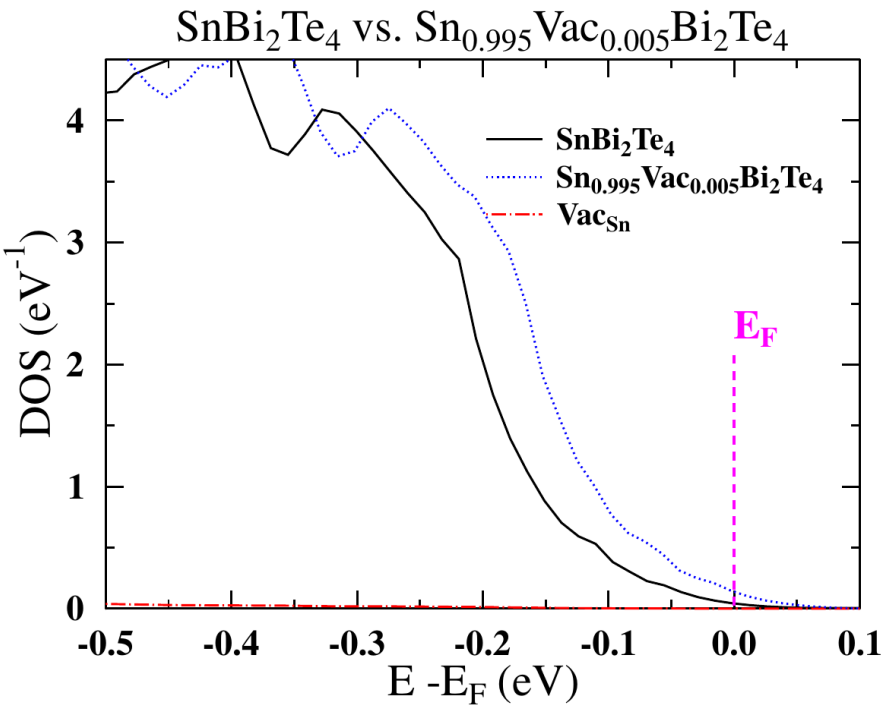

Figure S22. Effect of Sn vacancies on the density of states of $SnBi_2Te_4$. Sn vacancy leads only to the rigid shift of the DOS with respect to the Fermi level, thus acting as a rigid-band-like acceptor, which cannot be responsible for the changes in the band structure and electronic band gap, necessary to explain the experimentally observed behavior of $\alpha(T)$. This supports the hypothesis that Sn_{Bi} antisite defects are the main type of defects in $SnBi_2Te_4$. Calculations were performed using the Korringa-Kohn-Rostoker method with the coherent potential approximation (S4) in the scalar-relativistic and spherical-potential approximations.

References

(S1) Zou, Y.-C.; Chen, Z.-G.; Zhang, E.; Kong, F.; Lu, Y.; Wang, L.; Drennan, J.; Wang, Z.; Xiu, F.; Cho, K.; Zou, J. Atomic disorders in layer structured topological insulator $SnBi_2Te_4$ nanoplates. *Nano Res.* **2017**, *11*, 696–706.

(S2) Adoubya, K.; Touré, A. A.; Kra, G.; J. Olivier-Fourcade, J.; Jumas, J.-C.; Vicente, C. P. Phase diagram and local environment of Sn and Te: SnTe-Bi and SnTe-Bi_2Te_3 systems. *C. R. Acad. Sci. Paris*, *Série IIc, Chimie / Chemistry* **2000**, 3, 51–58.

(S3) Sano, H.; Herber, R.H. On the Mössbauer parameters of Barium stannate. *J. Inorg. Nucl. Chem.* **1968**, 30, 409–413.

(S4) Bansil, A., Kaprzyk, S., Mijnarends, P. E., and Toboła, J. Electronic structure and magnetism of $Fe_{3-x}V_xX$ (X = Si, Ga, and Al) alloys by the KKR-CPA method. Phys. Rev. B **1999**, *60*, 13396.